



RESEARCH ARTICLE

Compressive-sensing swept-source optical coherence tomography angiography with reduced noise

Lingyun Wang¹  | Ziyue Chen¹ | Zhanyu Zhu^{1*} | Xiaojun Yu^{2*}  | Jianhua Mo^{1*}

¹School of Electronics and Information Engineering, Soochow University, Suzhou, China

²School of Automation, Northwestern Polytechnical University, Xi'an, China

*Correspondence

Zhanyu Zhu, School of Electronics and Information Engineering, Soochow University, Suzhou, China.
Email: zyzhu@suda.edu.cn

Xiaojun Yu, School of Automation, Northwestern Polytechnical University, Xi'an, China.
Email: xjyu@nwpu.edu.cn

Jianhua Mo, School of Electronics and Information Engineering, Soochow University, Suzhou, China.
Email: joshuamo@gmail.com

Funding information

Natural Science Foundation of Jiangsu Province, Grant/Award Number: BK20140365; National Natural Science Foundation of China, Grant/Award Number: 81401451

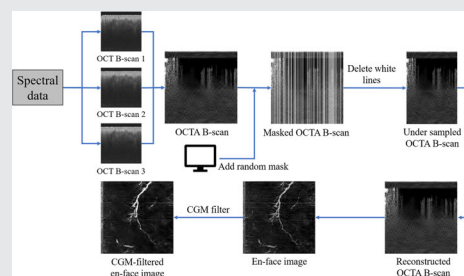
Abstract

Optical coherence tomography angiography (OCTA), as a functional extension of optical coherence tomography (OCT), has exhibited a great potential to aid in clinical diagnostics. Currently, OCTA still suffers from motion artifact and noise. Therefore, in this article, we

propose to implement compressive sensing (CS) on B-scans to reduce motion artifact by increasing B-scan rate. Meanwhile, a noise reduction filter is specially designed by combining CS, Gaussian filter and median filter. Specially, CS filtering is realized by averaging multiple CS repetitions on en-face OCTA images with varied sampling functions. The method is evaluated on in vivo OCTA images of human skin. The results show that vasculature structures can be reconstructed well through CS on B-scans with a sampling rate of 70%. Moreover, the noise can be significantly eliminated by the developed filter. This implies that our method has a good potential to expedite OCTA imaging and improve the image quality.

KEYWORDS

compressive sensing, motion artifact, noise reduction, optical coherence tomography angiography



1 | INTRODUCTION

Optical coherence tomography (OCT) is a newly developed optical imaging technique that can achieve high-resolution tomographic imaging of biological tissues [1].

Abbreviations: AD-OCT, amplitude-decorrelation OCT; BP, basis pursuit; CS, compressive sensing; D-OCT, Doppler OCT; FDML, Fourier-domain mode-locked; IHT, iterative hard thresholding; MRI, magnetic resonance imaging; OCT, optical coherence tomography; OCTA, optical coherence tomography angiography; OMP, orthogonal matching pursuit; PV-OCT, phase-variance OCT; SAR, synthetic aperture radar; SNR, signal-to-noise ratio; SS-OCT, swept-source OCT; SV-OCT, speckle-variance OCT.

In recent years, it has been widely accepted as a diagnostic tool for ophthalmic diseases in clinic. Optical coherence tomography angiography (OCTA), as an important functional extension of OCT, can produce three-dimensional vasculature image of human tissue and has found good applications in ophthalmology and dermatology [2–8]. OCTA utilizes the blood cell motion as the imaging contrast and vasculature structures are selectively imaged by analyzing the dynamic amplitude or phase information of OCT signals acquired consecutively at the same location of tissues [7, 9, 10]. Since no exogenous contrast agent is needed, OCTA is noninvasive [11]. In contrast, the current prevailing clinical angiography technique-

fluorescence angiography requires the use of extraneous fluorescent agent. Moreover, OCTA has the potential to perform velocity measurement of blood flow which is diagnostically useful [12].

At present, OCTA can be categorized into two types: phase-based and amplitude-based. The phase-based methods include Doppler OCT (D-OCT) and phase-variance OCT (PV-OCT) [10, 13]. The amplitude-based methods include amplitude-decorrelation OCT (AD-OCT) and speckle-variance OCT (SV-OCT) [7, 14]. Obviously, PV-OCT, AD-OCT and SV-OCT require multiple A-scans at the same location in the tissue, resulting in a longer imaging time. This will cause more occurrence of motion-induced artifact. Specifically, a sudden motion of tissue will cause the entire tissue to behave like a blood motion during the OCTA process and as a result, the vessels will be broken in OCTA image [15]. The entire OCTA B-scan appears to be bright which turns out to be white stripes in en-face OCTA images [16]. This further leads to challenges in analyzing vasculature image and extracting diagnostic features accurately [15, 17]. For example, the white stripes are likely to be segmented as blood vessels when performing vessel segmentation for quantitative analysis of tissue vasculature structure. To avoid or reduce the motion-induced artifacts, high-speed CMOS cameras/spectrometer for SD-OCT and high-speed wavelength-swept light sources for SS-OCT are developed to expedite OCT A-scan [18–20]. Among high-speed OCT solutions, OCT with the use of Fourier-domain mode-locked (FDML) lasers have shown to be able to achieve the fastest A-scan rate up to 3.35 MHz at 1060 nm [21]. However, this method is costly and pay the price of a reduced signal-to-noise ratio (SNR) due to the reduced integration time of the detector corresponding to the A-scan rate. Another solution for the motion artifact in ophthalmology is eye tracking technique, which however will complicate the whole system and increase the system cost. Lastly, software motion correction has been proposed to eliminate the motion artifact in postprocessing [2, 15]. However, this may sacrifice the valid field of view.

In addition, another issue needs to be addressed for OCTA imaging is the noise due to multiple scattering and speckle effects. More specifically, those noises cause the amplitude decorrelation of static tissue to be nonzero which smears the contrast of blood motion against the background in OCTA image. As a result, this may degrade the performance of vessel segmentation and eventually reduce the accuracy of quantitative analysis on vessels. In addition, the noise inside the vessel body may destroy the internal connectivity of the blood vessel (vascular fragmentation) which makes an accurate judgment on the vasculature structure more difficult for

clinicians. Thus, noise removal has received many research efforts in OCTA field. Digital filters are generally used to improve the image quality [22–24]. Buades et al. proposed a nonlocal means filter to reduce noise while preserving image details [25]. Lee et al. used Hessian analysis-based shape filter for OCTA flow contrast enhancement [26]. Oliveira et al. combined matched filter, Frangi's filter and Gabor wavelet filter to enhance the images [27]. Liu et al. utilized gamma transformation to enhance the image and then used combined collaborative filter and shock filter to smooth and sharpen the image [28]. Although digital filters achieve good results in image denoising, they face the challenge of preserving edges while reducing the noise [29].

Thus, in this study, we propose to use compressive-sensing (CS) technique to increase the OCTA imaging speed as well as to reduce the noise. To the best of our knowledge, CS technique has been introduced to OCT, and however not applied to OCTA yet. In principle, CS can achieve an image reconstruction with a high fidelity under a sub-Nyquist sampling if the object has a sparse representation. This under-sampling process can effectively reduce the measurement time as well as the amount of data [30]. In recent years, CS has been widely studied and applied to synthetic aperture radar (SAR) imaging, magnetic resonance imaging (MRI), OCT and so on [31–36]. In theory, CS can not only reduce the amount of data but also denoise since the small coefficients are suppressed in the process of reconstruction [37, 38]. For example, Xu et al. proposed modified CS-based averaging method to increase the image quality [39]. Later, Leportier et al. used a combination of CS with other filters to reduce noise [29]. Luo et al. demonstrated that five times CS averaging method offers an image quality and depth resolution similar to those obtained using the conventional averaging method [34]. As compared with those conventional noise reduction filters, CS-based denoising exhibits an advantage of better preserving the sharpness of the image during denoising process [29]. In this paper, we aimed to improve the OCTA image quality by combining CS with the traditional digital filters.

The principle of our method is to conduct CS on B-scans to increase the acquisition speed by reducing the amount of image data to be measured. Afterward, a CS filter is developed for noise reduction by averaging multiple en-face OCTA images which are generated by repeating CS on en-face images with varied sampling functions. Finally, two filters, that is, Gaussian filter and median filter, are implemented to further denoise the image. This method is evaluated on in vivo OCTA image of human skin.

2 | MATERIALS AND METHODS

2.1 | SS-OCTA imaging system

In this work, a swept-source OCT (SS-OCT) was built in lab for in vivo clinical measurement. The study was approved by the Human Research Ethics Committee of the First Affiliated Hospital of Soochow University (Suzhou, China), and the research was conducted with the principles embodied in the Declaration of Helsinki and in accordance with local statutory requirements. As shown in Figure 1A, the system works based on Michelson interferometer. The light source's output (SS-OCT 1060, Axsun Technology Inc, Billerica, MA) sweeps around 1060 nm with a bandwidth of about 110 nm at 100 kHz. The output light is split into two parts by a 50/50 fiber coupler, entering the reference arm and the sample arm, respectively. The reference arm consists of a pair of collimators and a pair of mirrors which are used to build a one-way light propagation path. The sampling arm is constructed with a collimating lens (F280APC-1064, Thorlabs, Newtown, NJ), a scanning galvanometer (GVSM002/M, Thorlabs, Newtown, NJ), an achromatic lens (AC254-060-B-ML, Thorlabs, Newtown, NJ) and an optical glass window (WG10530-B, Thorlabs, Newtown, NJ). The backscattered light reflected from the two arms interferes at a 50/50 fiber coupler, and the interference signal is detected by a balanced detector (PDB471C, Thorlabs, Newtown, NJ) and passes through a low-pass filter (SLP-150+, Mini-circuits, Brooklyn, NY) which

filters out the signal with a frequency higher than 155 MHz, and eventually is recorded in the computer through a 12-bit dual-channel data acquisition card (ATS9351, AlazarTech, Austin, TX). The scanning of B-scan is realized by a 16-bit high-speed analog output device (PCIe-6363, National Instruments, Austin, TX) outputting the analog signal to drive the galvanometer. To ease the clinical measurement, a handheld probe is fabricated by three-dimensional printing as described in Figure 1B. The axial and lateral resolutions of the system in air are approximately 11 and 20 μm , and the imaging depth in air is approximately 3.78 mm.

At present, we have not implemented random sampling into OCT beam scanning and thus a virtual random sampling is carried out on the full-sampled image in post-processing as illustrated in Figure 2. First, the SS-OCTA imaging system conducts a complete OCTA measurement, including three repeated OCT B-scans at the same position. Then, three cross-sectional intensity images are produced by the inverse fast Fourier transform. Subsequently, speckle variance is calculated over these three intensity images to obtain an OCTA B-scan. Next, a random mask is generated in computer according to the preset sampling rate to simulate the random sampling of an OCTA B-scan along the lateral dimension to obtain an under-sampled OCTA B-scan. For example, to under-sample an image with a rate of 70%, the computer will create a two-dimensional matrix with the same size as the image, of which 70% of the columns are set to be one and the rest to be zero. Moreover, the columns with the

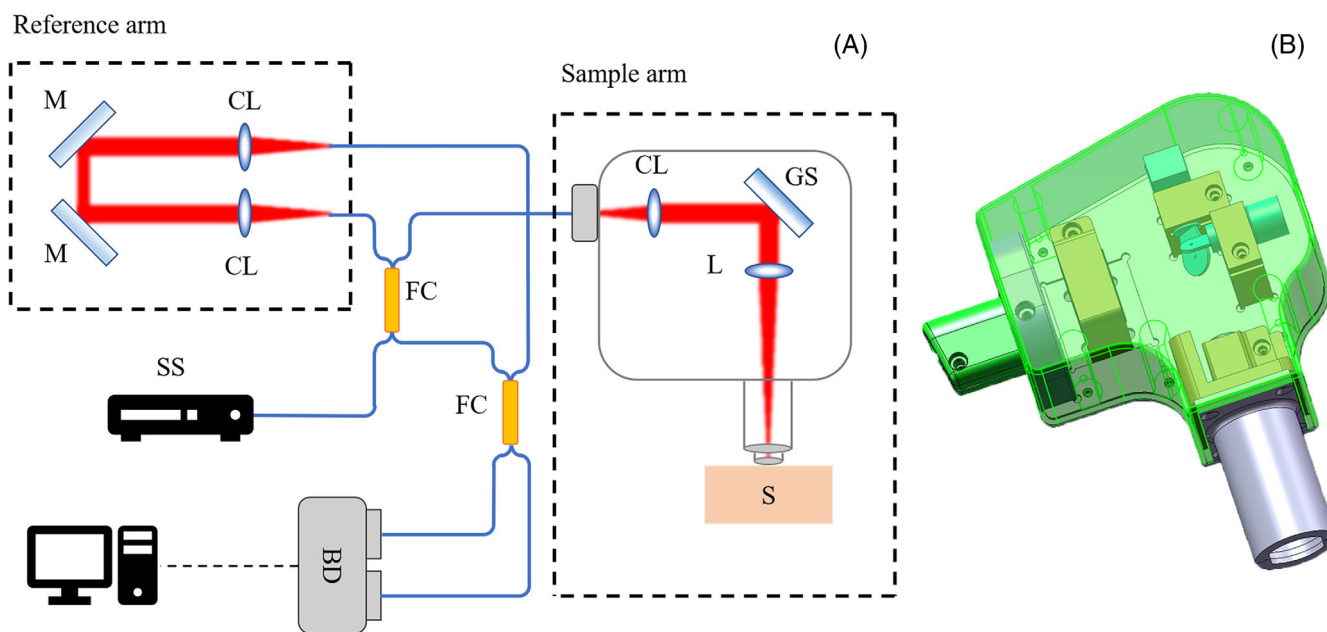


FIGURE 1 (A) Schematic of the swept-source OCTA imaging system. (B) Mechanical drawing of the handheld OCT probe. BD, balanced photodetector; CL, collimator; FC, fiber coupler; GS, galvo scanner; L, lens; M, mirror; S, sample; SS, swept source

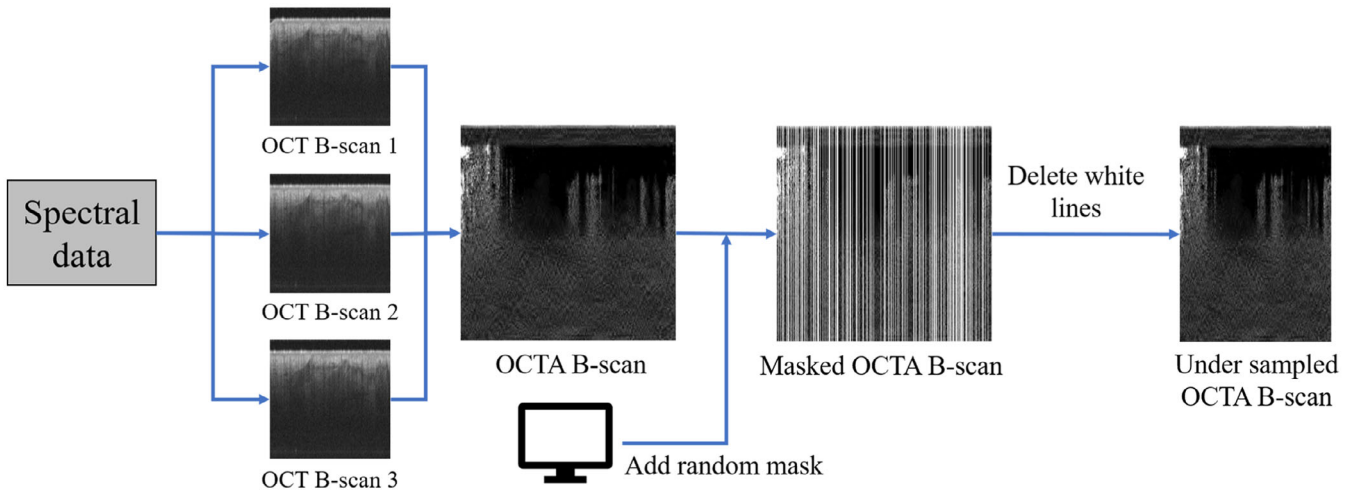


FIGURE 2 Flowchart of the computer simulation of random sampling

value of zero are distributed randomly along the lateral dimension. Then, the image is multiplied with the mask and in the resulted image, the columns filled with the element of zero are deleted to produce the under-sampled image. It should be noted that each column (A-scan) in OCT B-scan or OCTA B-scan is irrelevant throughout the processing, and it is reasonable to simulate the random sampling along the fast axis.

2.2 | B-scan compressive sensing

In OCTA imaging, one B-scan consists of N A-scans with a size of $N \times 1$, and one C-scan consists of N B-scans with a size of $N \times N$. Random sampling is conducted along the fast-scanning axis for each B-scan and the amount of A-scan in each B-scan is reduced from N to M . Let y represent randomly sampled observations whose size is $M \times 1$ in the horizontal direction, and x represent the expected B-scan data whose size is $N \times 1$ in the horizontal direction. Implementing compressive sensing requires data to be sparse and so the data can be transformed into the sparse domain. Let $x = \psi s$, where ψ is a sparse basis matrix and s is a sparse coefficient (Figure 3). Then, the process of compressive-sensing reconstruction can be expressed as:

$$\text{Minimize } \|s\|_1 \text{ subject to } \|\phi \psi s - y\|_2 < \epsilon \quad (1)$$

where ϕ is the observation matrix representing the random sampling function. The observation matrix ϕ and the sparse basis matrix ψ strictly satisfy the restricted isometric property [40]. ϵ is used to control the truncation error of image reconstruction, which is related to the noise of the image. The larger the value, the better the

denoising effect but the worse the quality of the reconstructed blood vessels. In general, it is necessary to find a suitable value to compromise between the data reduction and the image detail preservation. The notation $\|m\|_1$ and $\|m\|_2$ are the l_1 and l_2 norms respectively.

The sparse basis matrix ψ often adopts wavelet transform matrix and Fourier matrix. It has been found that the image reconstructed by wavelet transform is sharper while the image reconstructed by Fourier transform is smoother [41]. To keep the edges of the blood vessels well, wavelet transform matrix is used for image reconstruction in this study. Various methods have been proposed to solve Equation (1) such as basis pursuit (BP), iterative hard thresholding (IHT), and orthogonal matching pursuit (OMP) [40, 42, 43]. Among those methods, OMP algorithm exhibits a quick converge as the residuals are always orthogonal to the selected atoms. Considering OCTA imaging requires a large amount of data, to have a time cost-effective image reconstruction, OMP algorithm is employed to solve Equation (1). The reconstruction process is repeated for each row of the under-sampled B-scan to get the full reconstructed B-scan image.

Since only part of the data is used in random sampling, in theory, CS is capable of increasing the OCTA imaging speed. At the same time, due to the minimization of the l_1 norm in the reconstruction process, many small coefficients are suppressed which can help reduce the noise in the reconstructed image.

2.3 | Denoising algorithm

As discussed above, CS has the capability of denoising. Thus, a denoising algorithm is designed by combining CS

FIGURE 3 Schematic diagram of compressive sensing. x , y and s represent the expected value, the observed value and the sparse coefficient, respectively. ϕ represents the observation matrix, which projects the high-dimensional signal x to the low-latitude space. ψ is the sparse base matrix, which can sparsely represent the expected value x to obtain the sparse coefficient s

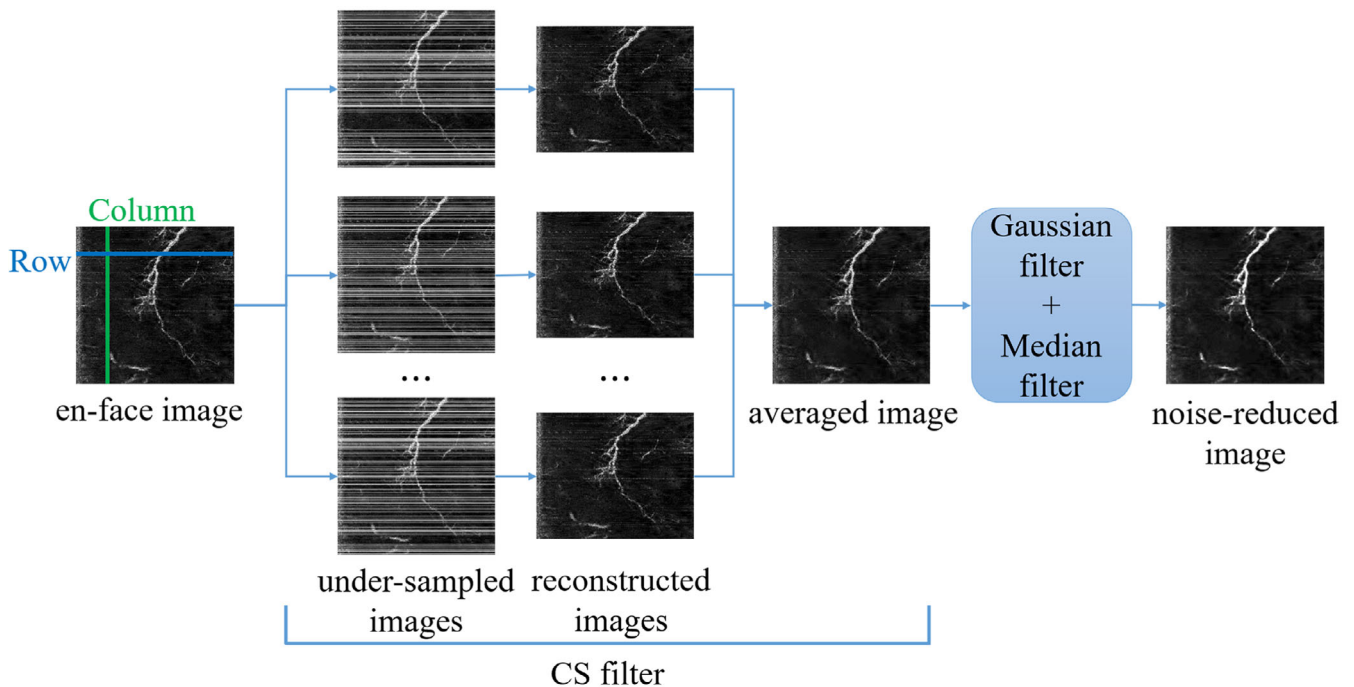
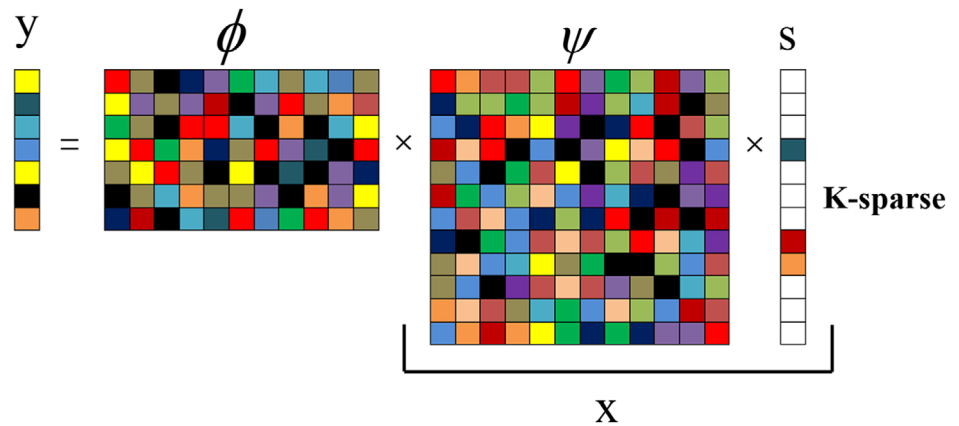


FIGURE 4 Flowchart of CGM filter process

filter with Gaussian filter and median filter, called CGM filter, dedicated to reducing the noise in en-face OCTA image. It consists of three steps as illustrated in Figure 4. First, CS implementation is repeated multiple times with varied random sampling functions along slow axis on en-face OCTA image. CS is applied to all the columns with the same sampling function (random mask) as shown in Figure 4. This random sampling process is similar as described in Section 2.1. The difference is that the random sampling is performed along the slow axis for CS filter while along the fast axis for B-scan CS. Note that the reason why the sampling is along the slow axis is that this may eliminate the row stripe due to background motion. In detail, if the motion-induced artificial lines are partially sampled or even not sampled, they will have

a small probability to be recovered in the reconstruction. Second, the images reconstructed with different random sampling functions are averaged to create a new image with reduced noise. The process is defined as CS filter. The resulted noise reduction can be explained by the fact that different random sampling function results in an uncorrelated noise distribution in the reconstructed image.

Next, to further enhance the SNR of the OCTA image, two conventional filters, that is, Gaussian filter and median filter are applied to the images after CS filtering. Gaussian filter realizes a noise reduction by convoluting a Gaussian function with the image and has been widely used in image processing. It can smooth out the noise, and however, the vanishing of edges will be an issue

when large variance is used in the filter function [44]. Median filter is a nonlinear filter process which replaces the value of the targeted pixel with the median of all pixel values in the preset window. It can preserve the edge when reducing noise, especially impulse noise [45]. For OCTA image, if it is applied to the original en-face OCTA images before CS filtering, it may cause a thinning of the blood vessels which will decrease the accuracy of the quantitative analysis on the vasculature structures. Therefore, Gaussian filter and median filter are implemented in sequence following CS filtering. Gaussian filter can improve the connectivity of the blood vessels (black spots inside vessels are significantly reduced). The improved connectivity of the blood vessel can effectively prevent the fragmented blood vessel edges from being removed by the subsequent implementation of median filter.

2.4 | Evaluation metrics

In this study, we used four metrics to evaluate the image quality, including contrast-to-noise ratio (CNR), equivalent numbers of looks (ENL), signal-to-noise ratio (SNR) and local contrast (LC) [29, 38, 39]. They are defined as follows:

$$\text{CNR} = 20 \times \log_{10} \frac{\mu_o - \mu_b}{\sigma_b} \quad (2)$$

$$\text{ENL} = \mu_b^2 / \sigma_b^2 \quad (3)$$

$$\text{SNR} = 20 \times \log_{10} \frac{\mu_o}{\sigma_b} \quad (4)$$

$$\text{LC} = \mu_o / \mu_b \quad (5)$$

where μ_o is the mean gray value of the vessel area, μ_b is the mean gray value of the background area, σ_b is the standard deviation of the background's gray value, CNR and LC reflect the contrast of blood vessels in the image (the degree of visualization of blood vessels), ENL can measure the smoothness of a uniform area, which is used to reflect the smoothness of the background and SNR is used to measure the denoising effect.

3 | RESULTS AND DISCUSSION

3.1 | Data reduction

This study is to explore the feasibility of utilizing CS to increase the imaging rate of OCTA by reconstructing the image based on under-sampled data. However, as the

sampling rate decreases, the correlation of the reconstructed image with the image obtained by full sampling gets lower. Thus, a compromise must be made between the sampling rate and the correlation above.

To determine the optimal sampling rate, the CS-reconstructed images with a sampling rate of from 30% to 90% with a step size of 10% are evaluated as described in Figure 5. The CS is implemented on B-scans and then the en-face image is created by single-pixel projection at a certain depth. The image was acquired from the chest of a young female patient who underwent a laser scar removal surgery. For the sampling rate of 30%, it is hard to recognize the vessel morphological structure in the reconstructed image (Figure 5A), that is, the junctions of the vessels in the red rectangle. When the sampling rate is increased from 30% to 70%, the visualization of the vessel structure is significantly improved. Similar observation can be obtained in the OCTA B-scan as seen in Figure 6. In addition, when the sampling rate is further increased from 70%, the improvement on the vessel integrity in the reconstructed image becomes subtle and hardly recognizable. Besides, it is found that in those non-vessel areas, the image reconstructed with the sampling rate above 70% shows less noise as compared with the full-sampled image. This can be explained by the denoising capability of CS.

To quantify the performance of CS with various sampling rates, the correlation coefficient of the reconstructed image with the full-sampled image was calculated on both OCTA B-scans and en-face images as depicted in Figure 7 which can reflect the accuracy of the image reconstruction by CS. Overall, the increase of the sampling rate is accompanied with an increase of the correlation coefficient, which behaves like a logarithmic function. The correlation coefficient is elevated approximately from 0.5 to 0.78 when the sampling rate is increased from 30% to 70%. The corresponding reconstructed vessels with a sampling rate of 70% look almost identical to that in the full-sampled image. This means that the correlation coefficient of 0.78 can effectively reflect a good CS reconstruction quality of sparse vessels. In addition, the correlation function for B-scans exhibits a larger fluctuation than that for en-face image, especially at low sampling rate. This can be accounted for by the fact that in each B-scan, the vessel area takes up a smaller portion of the entire image and the noise (non-vessel area) makes more contribution to the correlation calculation as compared with the en-face image.

3.2 | Noise reduction

Noise reduction based on CS has been introduced to OCT [34]. It should be noted that the sampling process is a random function. Thus, for each repetition of the CS-

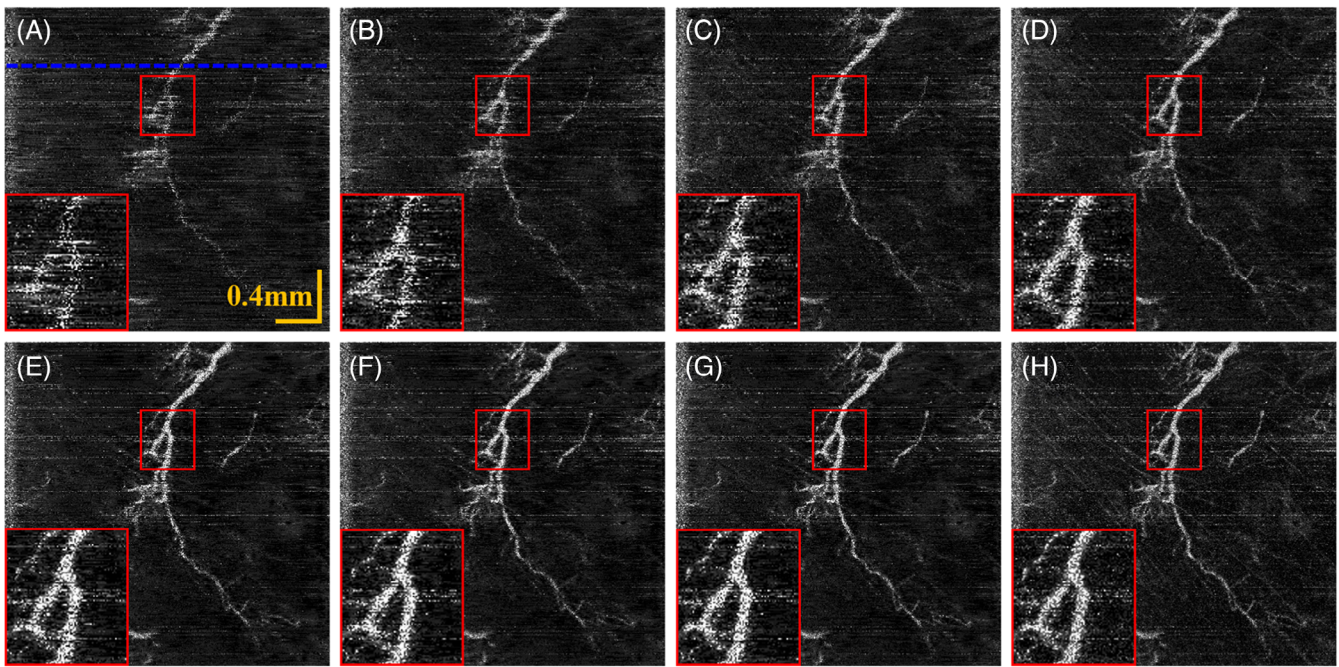


FIGURE 5 En-face OCTA images at different sampling rates, (A–G) are the en-face OCTA images when the sampling rate is from 30% to 90% with a step size of 10%, (H) is the fully sampled en-face OCTA image

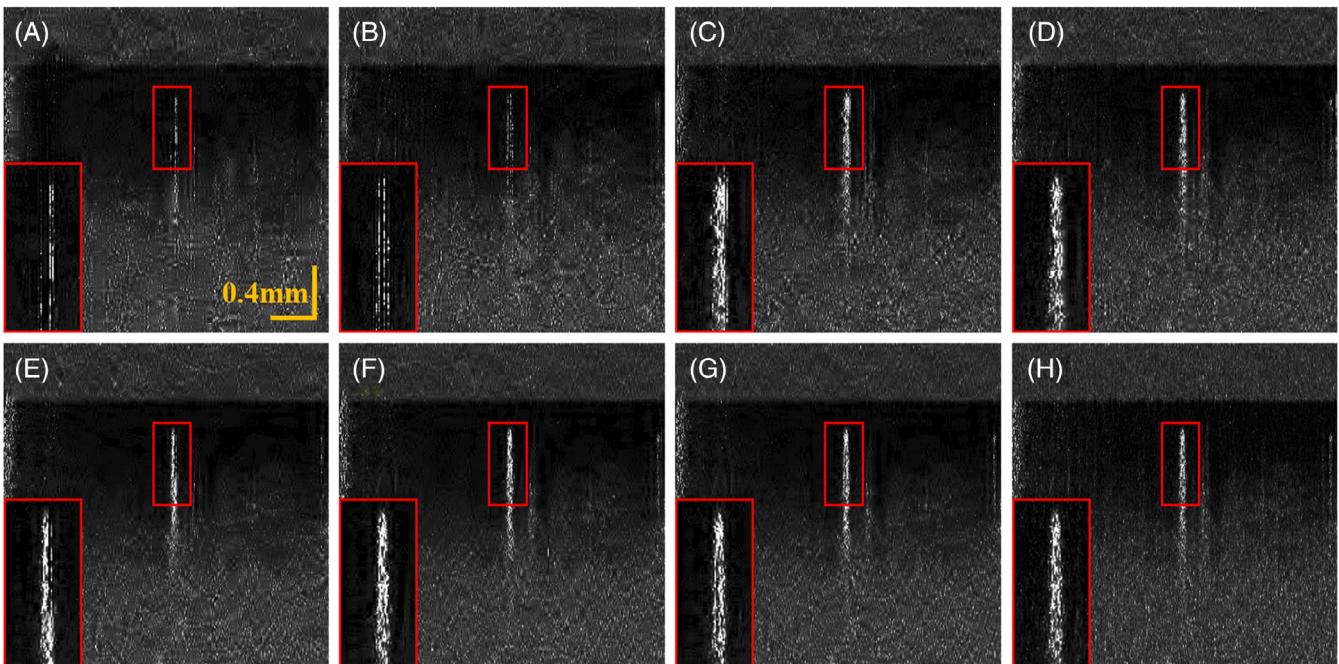


FIGURE 6 OCTA B-scan images at different sampling rates, (A–G) are the OCTA B-scan images when the sampling rate is from 30% to 90% with a step size of 10%, (H) is the fully sampled OCTA B-scan image. This B-scan is along the blue dashed line in Figure 5A

reconstruction based on different random sampling function, the noise exhibits a different distribution. This will enable a noise reduction through averaging multiple repetitions. In this study, this CS-based noise reduction is implemented on en-face image. The performance of this CS filter is mainly dependent on the sampling rate and

the number of repetitions to be averaged, which therefore need to be optimized.

In theory, the sampling rate impacts the reconstructed image from two aspects. One is that the reconstructed image correlates better with the full-sampled image when a higher sampling rate is used. From this point of view, a

high sampling rate is desired. On the other hand, noise distribution varies more among repeated reconstructions with a lower sampling rate. Apparently, with a larger noise distribution variation, averaging multiple repetitions will yield a larger noise reduction. In practice, the reconstructed image quality is preferentially used to determine the minimal sampling rate. For an en-face OCTA image with a sparse vasculature structure, the non-sampled vessel will have a larger probability to be missed in the reconstructed image when

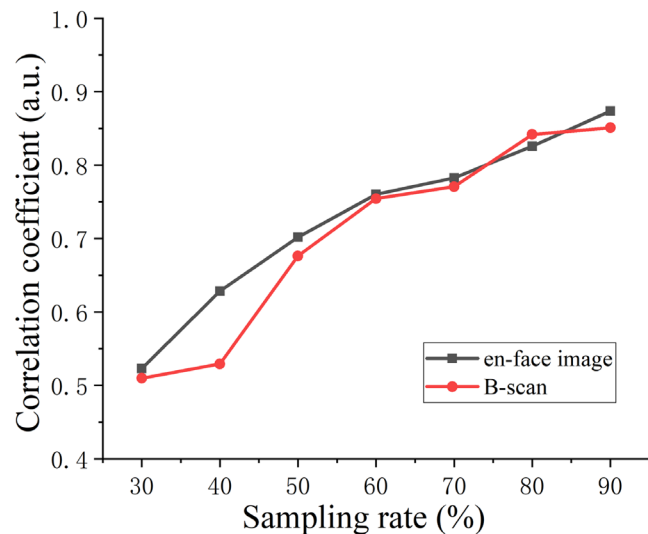


FIGURE 7 Correlation coefficients at different sampling rates

the sampling rate is decreased. To obtain an acceptable low sampling rate, the images reconstructed with an en-face sampling rate from 30% to 90% with a step size of 10% were evaluated. The correlation between each reconstruction and the full-sampled image was calculated and for each sampling rate, the reconstruction was repeated five times and consequently five correlation coefficients will be produced and eventually averaged. The mean correlation coefficients are 0.34, 0.39, 0.47, 0.55, 0.62, 0.72 and 0.85 for the sampling rates of 30% to 90% with a step size of 10%, respectively. It needs to be pointed out that the correlation coefficient is computed over the entire image including both vessels and background (non-vessel area). Thus, when only considering the vessels, a sampling rate of 70% is high enough to obtain a good reconstruction of vessels and therefore is adopted as the en-face sampling rate for the following noise reduction work.

Next, the optimal number of reconstruction repetitions for averaging is experimentally determined. Figure 8 describes the images generated by averaging one to seven repetitions. It is observed that upon one CS reconstruction, the image exhibits a smoother background than the full-sampled image. The corresponding SNR is improved from 21.75 dB to 22.12 dB. This demonstrates the noise-filtering capability of CS reconstruction. The background area gets smoother when averaging two and three repeated reconstructions. The SNR is further improved to 23.54 and 24.32 dB. However, it is hard to recognize that

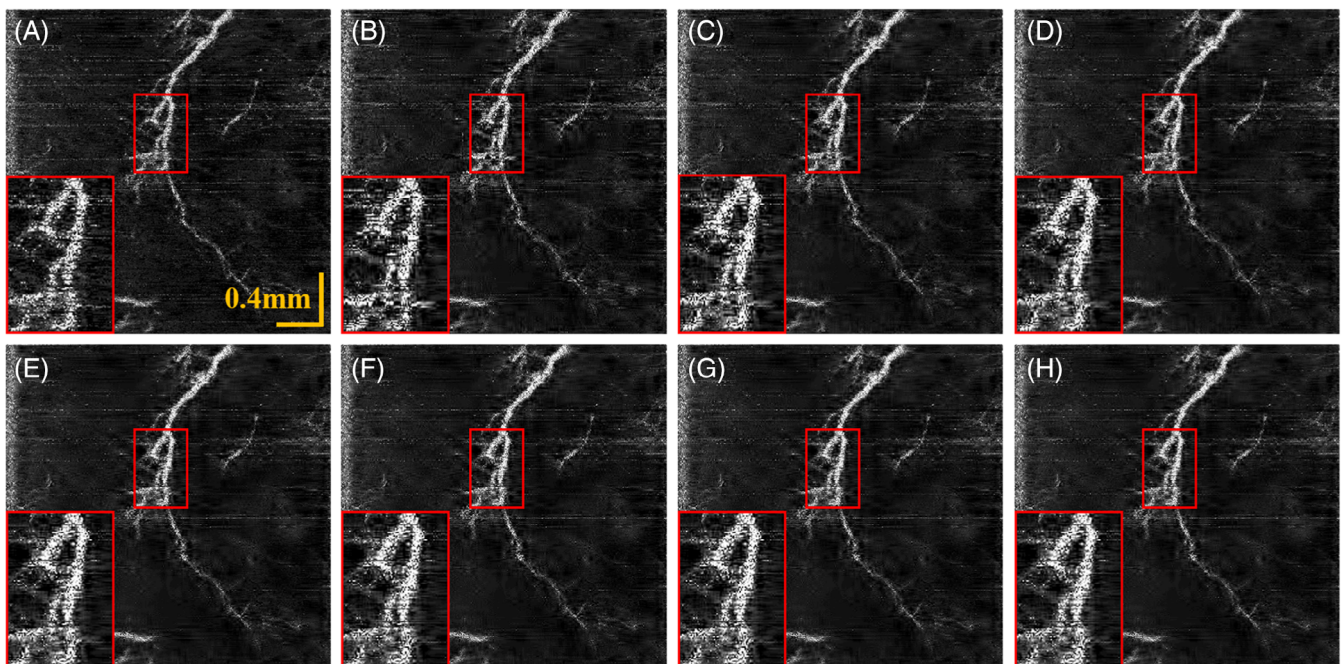


FIGURE 8 (A) En-face OCTA image with a sampling rate of 100%. (B–H) are the images generated by averaging the repeated CS-reconstructed images with an en-face sampling rate of 70%. The corresponding number of repetitions is from one to seven, respectively. The SNRs of (A–H) are 21.75, 22.12, 23.54, 24.32, 24.46, 24.32, 24.21 and 24.49, respectively

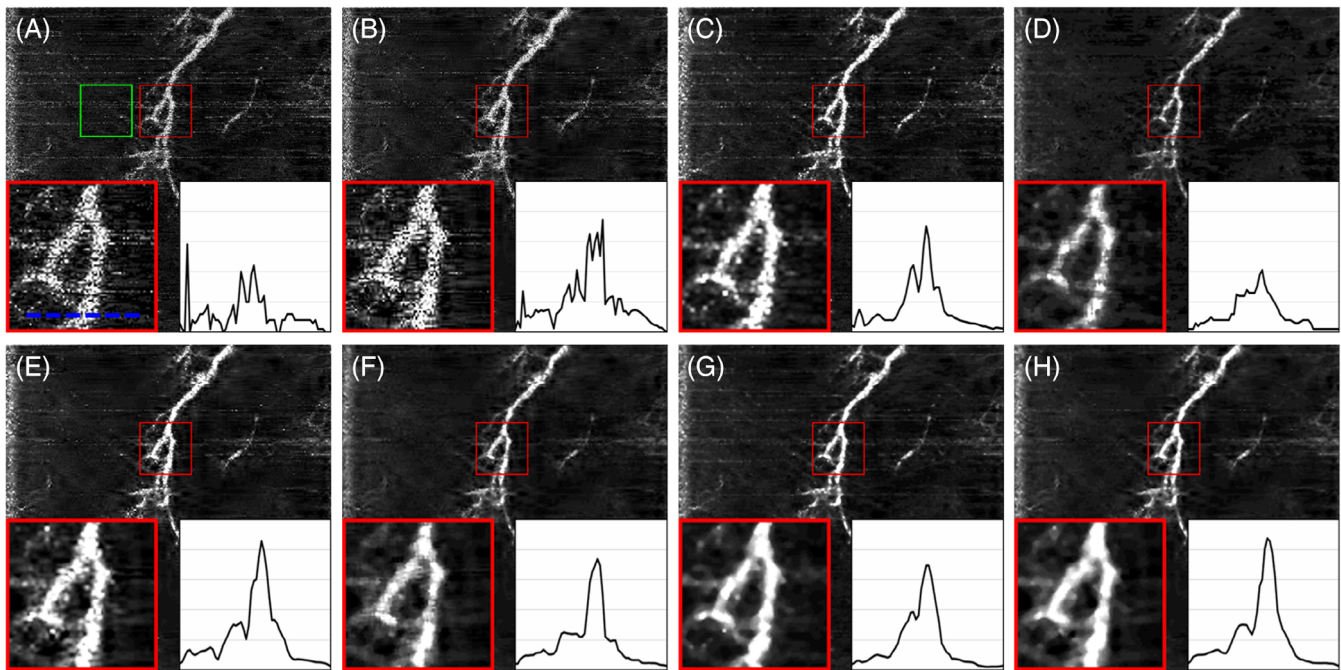


FIGURE 9 Evaluation of noise reduction by various filters and their combinations: (A) en-face image constructed with CS-reconstructed B-scans. (B–H) various filters performed on (A), including (B)-CS filter, (C)-Gaussian filter, (D)-median filter, (E)-combined CS filter and Gaussian filter, (F)-combined CS filter and median filter, (G)-combined Gaussian filter and median filter, and (H)-combination of all the three filters above (CGM filter). Note that the sampling rate of CS reconstruction is 70% both for B-scan and en-face image. CS filter is an average of three repetitions of CS-reconstruction on en-face image. The bottom right corner of each image is the intensity profile of the blood vessel marked by the blue dashed line in (A) and its abscissa range is 221 to 280 pixels and ordinate range is 0–50

TABLE 1 Evaluation metrics of figures A–H in Figure 9

Method	CNR (dB)	ENL	SNR (dB)	LC
No filter	19.23	0.71	20.00	11.84
CS filter	23.32	1.74	24.07	12.10
Gaussian filter	24.76	2.71	25.55	11.52
Median filter	25.72	7.12	26.84	8.24
CS filter + Gaussian filter	26.99	4.34	27.76	11.74
CS filter + Median filter	26.52	6.55	27.51	9.27
Gaussian filter + Median filter	26.96	5.17	27.80	10.80
CS filter + Gaussian filter + Median filter (CGM)	27.83	6.19	28.66	10.90

the background becomes smoother when the number of the repeated reconstructions for averaging continues to be increased. The SNR seems to be stabilized around 23.3 dB. This indicates that averaging three repeated reconstructions can provide an optimal compromise between noise reduction and computation cost and therefore will be used for the following CGM filter process.

As shown in Figure 8, although the background is smoothed by CS filtering, the vessel body remains noisy, and its edge is not sharp. Consequently, Gaussian filter and median filter are applied to improve the quality of

vessel image. The images resulted from CS filtering, Gaussian filtering and median filtering are described in Figure 9B–D, respectively. It is obvious that Gaussian filter performs best on noise reduction while CS filtering is the worst. Median filter achieves a good elimination of the horizontal thin lines. To better evaluate the performance of the noise reduction, an intensity profile was plotted as an example in the bottom right corner of each figure. Next, these three filters mentioned above are combined in all four possible ways to further reduce the noise as illustrated in Figure 9E–H. It is seen that combining

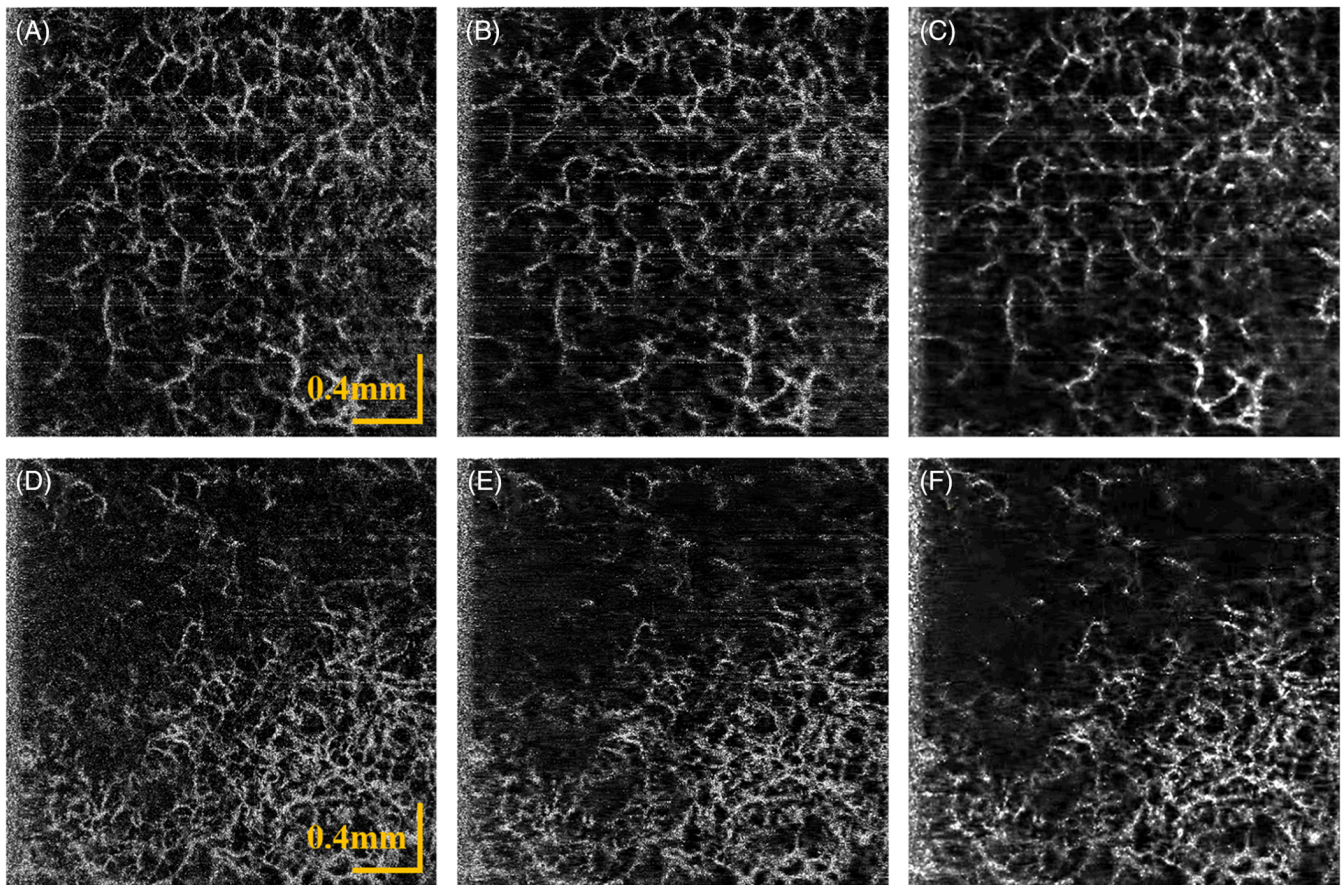


FIGURE 10 Evaluation of CS reconstruction and CGM filter on en-face images of human ear and cheek: (A) raw image of ear. (B–C) the corresponding CS-reconstructed image and CGM-filtered image. (D) raw image of cheek. (E–F) the corresponding CS-reconstructed image and CGM-filtered image

two of those three filters can make the intensity profile to be single-peak shape and smoother. As for the combination of all the three filters, little significant improvement can be observed on the intensity profile. Therefore, four metrics, including CNR, ENL, SNR and LC are computed to quantify the performance of the methods depicted in Figure 9 as summarized in Table 1. CGM filter yields the highest CNR, SNR and the third highest ENL (choose the blood vessels in the red rectangle as the signal and the area in the green rectangle as the noise to calculate the metrics). As for LC, although CGM filter is inferior to any individual use of those three filters, it is superior to combination of CS filter and median filter, and combination of Gaussian filter and median filter. Overall, it is reasonable to consider CMG filter as the optimal one.

From the discussion above, the processing protocol of our proposed method is finalized as: A, CS reconstruction with a sampling rate of 70% on each B-scan. B, Implementation of CS filter with a sampling rate of 70%, Gaussian filter and median filter in sequence on en-face OCTA images. To further demonstrate the robustness of this method, it was tested on two OCTA images acquired

from two different parts of human skin in vivo, including the ear and the cheek of a patient who underwent a burn injury. Figure 10A, D depict the raw en-face OCTA images. The corresponding images produced exclusively from CS reconstruction on each B-scan are presented in Figure 10B, E. The vessel structures are well reconstructed, indicating that CS reconstruction on B-scans can reduce the size of original data without losing the object's structure. The image quality is then improved significantly by CGM filter as illustrated in Figure 10C, F, especially in terms of SNR and image contrast, demonstrating the efficacy of CGM filter.

4 | CONCLUSION

In this article, we proposed a new technique based on CS dedicated to accelerating OCTA imaging as well as improving the image quality. To the best of our knowledge, this is the first application of CS to OCTA. The designed technique was evaluated on in vivo OCTA images of human skin. The results demonstrated that raw OCT can be

reduced by a factor of 0.7 through CS-reconstruction on B-scans while vessel structures are maintained well in the reconstructed images. This can expediate the imaging and consequently reduce the motion-induced artifact. Moreover, the image quality can be significantly improved by combining CS filter with Gaussian filter and median filter. This can potentially contribute to improve the quantitative analysis of vasculature structures and eventually improve the clinic utility of OCTA imaging in disease diagnosis and treatment assessment.

In the future, the sparse sampling will be realized in practical OCT imaging by designing the optical beam scanning mechanism and evaluating the performance of the technique in clinic in real time. In addition, it must be admitted that the current method is only well suited for vasculature image as it exhibits a sparse structure. Thus, to extend the application of this method, the algorithm needs to be improved to have a good reconstruction of non-sparse image.

ACKNOWLEDGMENTS

The research reported in this article was supported by National Natural Science Foundation of China (81401451) and Natural Science Foundation of Jiangsu Province (BK20140365).

CONFLICT OF INTEREST

The authors declare no financial or commercial conflict of interest.

DATA AVAILABILITY STATEMENT

Data underlying the results presented in this paper are not publicly available at this time but may be obtained from the authors upon reasonable request.

ORCID

Lingyun Wang  <https://orcid.org/0000-0002-9380-6032>

Xiaojun Yu  <https://orcid.org/0000-0001-7361-0780>

REFERENCES

- [1] J. M. Schmitt, *IEEE J. Sel. Top. Quant.* **1999**, 5(4), 1205.
- [2] R. F. Spaide, J. G. Fujimoto, N. K. Waheed, S. R. Sadda, G. Staurengi, *Prog. Retin. Eye Res.* **2018**, 64, 1.
- [3] C.-L. Chen, R. K. Wang, *Biomed. Opt. Express* **2017**, 8(2), 1056.
- [4] S. Makita, Y. Hong, M. Yamanari, T. Yatagai, Y. Yasuno, *Opt. Express* **2006**, 14(17), 7821.
- [5] M. Yamanari, M. Miura, Y. Yasuno, S. Makita, F. Jaillon, *Opt. Express* **2011**, 19(2), 1271.
- [6] R. K. Wang, S. L. Jacques, Z. Ma, S. Hurst, S. R. Hanson, A. Gruber, *Opt. Express* **2007**, 15(7), 4083.
- [7] Y. Jia, O. Tan, J. Tokayer, B. Potsaid, Y. Wang, J. J. Liu, M. F. Kraus, H. Subhash, J. G. Fujimoto, J. Hornegger, D. Huang, *Opt. Express* **2012**, 20(4), 4710.
- [8] M. Ulrich, L. Themstrup, N. de Carvalho, M. Manfredi, C. Grana, S. Ciardo, R. Kästle, J. Holmes, R. Whitehead, G. B. E. Jemec, *Dermatology* **2016**, 232(3), 298.
- [9] E. Jonathan, J. Enfield, M. J. Leahy, *J. Biophotonics* **2011**, 4(9), 583.
- [10] J. Fingler, D. Schwartz, C. Yang, S. E. Fraser, *Opt. Express* **2007**, 15(20), 12636.
- [11] R. F. Spaide, J. M. Klancnik, M. J. Cooney, *JAMA Ophthalmol.* **2015**, 133(1), 45.
- [12] B. Braaf, M. G. O. Gräfe, N. Uribe-Patarroyo, B. E. Bouma, B. J. Vakoc, J. F. de Boer, S. Donner, J. Weichsel, *High Resolution Imaging in Microscopy and Ophthalmology: New Frontiers in Biomedical Optics*. Cham: Springer; **2019**, p. 161.
- [13] Y. Li, J. Chen, Z. Chen, *Transl. Biophoton.* **2019**, 1(1–2), e201900005.
- [14] K. K. C. Lee, A. Mariampillai, X. Z. Joe, D. W. Cadotte, B. C. Wilson, B. A. Standish, V. X. D. Yang, *Biomed. Opt. Express* **2012**, 3(7), 1557.
- [15] E. C. Greig, J. S. Duker, N. K. Waheed, *Int. J. Retina Vitreous* **2020**, 6(1), 55.
- [16] A. Camino, M. Zhang, C. Dongye, A. D. Pechauer, T. S. Hwang, S. T. Bailey, B. Lujan, D. J. Wilson, D. Huang, Y. Jia, *Quant. Imaging Med. Surg.* **2016**, 6(4), 391.
- [17] G. R. Untracht, R. S. Matos, N. Dikaios, M. Bapir, A. K. Durrani, T. Butsabong, P. Campagnolo, D. D. Sampson, C. Heiss, D. M. Sampson, *PLoS One* **2021**, 16(12), e0261052.
- [18] D. Choi, H. Hiro-Oka, H. Furukawa, R. Yoshimura, M. Nakanishi, K. Shimizu, K. Ohbayashi, *Opt. Lett.* **2008**, 33(12), 1318.
- [19] C. Viehland, J. D. Li, A.-H. Dhalla, W. Raynor, L. Vajzovic, A. N. Kuo, C. Toth, J. A. Izatt, *Invest. Ophthalmol. Vis. Sci.* **2020**, 61(7), 3244.
- [20] I. Grulkowski, M. Gora, M. Szkulmowski, I. Gorczynska, D. Szigal, S. Marcos, A. Kowalczyk, M. Wojtkowski, *Opt. Express* **2009**, 17(6), 4842.
- [21] T. Klein, W. Wieser, L. Reznicek, A. Neubauer, A. Kampik, R. Huber, *Biomed. Opt. Express* **2013**, 4(10), 1890.
- [22] M. Chlebiej, I. Gorczynska, A. Rutkowski, J. Kluczewski, T. Grzona, E. Pijewska, B. L. Sikorski, A. Szkulmowska, M. Szkulmowski, *Biomed. Opt. Express* **2019**, 10(2), 1013.
- [23] J. Garcia-Sucerquia, J. A. H. Ramirez, D. V. Prieto, *Optik* **2005**, 116(1), 44.
- [24] A. Stern, V. Farber, A. Uzan, Yair Rivenson. in *Three-Dimensional Imaging, Visualization, and Display 2014*, International Society for Optics and Photonics, Baltimore, MD **2014**, p. 91170C.
- [25] A. Buades, B. Coll, J.-M. Morel, *Int. J. Comput. Vision* **2008**, 76(2), 123.
- [26] J. Lee, J. Y. Jiang, W. Wu, F. Lesage, D. A. Boas, *Biomed. Opt. Express* **2014**, 5(4), 1160.
- [27] W. S. Oliveira, J. V. Teixeira, T. I. Ren, G. D. C. Cavalcanti, J. Sijbers, *PLoS One* **2016**, 11(2), e0149943.
- [28] G. Liu, Z. Wang, G. Mu, P. Li, *J. Healthc. Eng.* **2018**, 2018, 7329548.
- [29] T. Lepotier, M.-C. Park, *Optim. Eng.* **2016**, 55, 12.
- [30] X. Liu, J. U. Kang, *Opt. Express* **2010**, 18(21), 22010.
- [31] M. Lustig, D. Donoho, J. M. Pauly, *Magn. Reson. Med.* **2007**, 58(6), 1182.
- [32] J. Wang, E. J. Chaney, E. Aksamitiene, M. Marjanovic, S. A. Boppart, *J. Phys. D Appl. Phys.* **2021**, 54, 29.

- [33] L. Chen, J. Liu, J. Cheng, H. Liu, H. Zhou, *Opt. Commun.* **2017**, 387, 117.
- [34] S. Luo, L. Huo, Q. Guo, H. Zhao, X. An, L. Zhou, H. Xie, J. Tang, X. Wang, H. Chen, *IEEE Photon. J.* **2018**, 10(1), 1.
- [35] Y. Ling, W. Meiniel, R. Singh-Moon, E. Angelini, J. C. Olivio-Marin, C. P. Hendon, *Opt. Express* **2019**, 27(2), 855.
- [36] X. X. Zhu, R. Bamler, *IEEE Signal Proc. Mag.* **2014**, 31(4), 51.
- [37] N. Zhang, T. Huo, C. Wang, T. Chen, J.-g. Zheng, P. Xue, *Opt. Lett.* **2012**, 37(15), 3075.
- [38] W. Liao, J. Hsieh, C. Wang, W. Zhang, S. Ai, Z. Peng, Z. Chen, B. He, X. Zhang, N. Zhang, B. Tang, P. Xue, *Opt. Lett.* **2019**, 44(12), 2955.
- [39] D. Xu, N. Vaswani, Y. Huang, J. U. Kang, *Opt. Lett.* **2012**, 37(20), 4209.
- [40] E. J. Candès, J. Romberg, T. Tao, *IEEE Trans. Inf. Theory* **2006**, 52(2), 489.
- [41] D. Xu, Y. Huang, J. U. Kang, *Biomed. Opt. Express* **2014**, 5(11), 3921.
- [42] T. Blumensath, M. E. Davies, *Appl. Comput. Harmon. A.* **2009**, 27(3), 265.
- [43] V. K. Goyal, A. K. Fletcher, S. Rangan, *IEEE Signal Proc. Mag.* **2008**, 25(2), 48.
- [44] Guang Deng, LW Cahill, in **1993** IEEE Conference Record Nuclear Science Symposium and Medical Imaging Conference, IEEE, San Francisco, CA, 1993, pp. 1615–1619.
- [45] T. Nodes, N. Gallagher, *IEEE Trans. Acoust* **1982**, 30(5), 739.

How to cite this article: L. Wang, Z. Chen, Z. Zhu, X. Yu, J. Mo, *J. Biophotonics* **2022**, e202200087. <https://doi.org/10.1002/jbio.202200087>